Research Square

Preprints are preliminary reports that have not undergone peer review.
They should not be considered conclusive, used to inform clinical practice,
or referenced by the media as validated information.

# Multiple b-value diffusion-weighted imaging for predicting lymphovascular space invasion and evaluating prognostic outcomes in endometrial carcinoma

**Lianze Du**
Weifang People's Hospital
**Xianli Sun**
Shandong Second Medical University
**Hongyang Yang**
Weifang People's Hospital
**Xintong Sui**
Sunshine Union Hospital
**Xiuwen Wu**
Shandong Second Medical University
**Puye Wu**
GE Healthcare
**Wenjuan Wang**
wangwj212@163.com

Weifang People's Hospital

**Research Article**

**Keywords:** Endometrial carcinoma, multi-b-value DWI, lymphovascular space invasion, predictive performance, prognostic outcomes

**Posted Date:** November 25th, 2026

**DOI:** https://doi.org/10.21203/rs.3.rs-11711816/v1

**License:** This work is licensed under a Creative Commons Attribution 4.0 International License.
Read Full License

**Additional Declarations:** No competing interests reported.

# Multiple b-value diffusion-weighted imaging for predicting lymphovascular space invasion and evaluating prognostic outcomes in endometrial carcinoma

**Abbreviations**

| | |
|---|---|
| ADC | Apparent diffusion coefficient |
| AICc | Corrected Akaike Information Criterion |
| AUC | Area under the curve |
| BMI | Body mass index |
| CI | Confidence interval |
| CTRW | Continuous-time random walk |
| D | Pure diffusion coefficient |
| D* | Pseudodiffusion coefficient |
| DDC | Distributed diffusion coefficient |
| DFS | Disease-free survival |
| DKI | Diffusion kurtosis imaging |
| EC | Endometrial carcinoma |
| FROC | Fractiona-order calculus |
| ICC | Intraclass correlation coefficient |
| MK | Mean kurtosis |
| MD | Mean diffusivity |
| MRI | Magnetic resonance imaging |
| MRE | Magnetic resonance elastography |

| | |
|---|---|
| LVSI | Lymph-vascular space invasion |
| OR | Odds ratio |
| OS | Overall survival |
| ROC | Receiver operating characteristic curve |
| ROI | Regions of interest |
| SEM | Stretched exponential model |
| VIF | Variance inflation factor |

## Abstract

**Purpose:** To systematically compare quantitative parameters derived from multiple diffusion models for preoperative Lymphovascular space invasion (LVSI) assessment and to identify independent imaging predictors of LVSI in EC.

**Material and methods:** A total of 113 consecutive patients with EC from hospital were enrolled. 15 diffusion parameters derived from 7 diffusion models, including DWI, diffusion kurtosis imaging (DKI), intravoxel incoherent motion (IVIM), stretched exponential model (SEM), continuous-time random walk (CTRW), fractional order calculus (FROC) and virtual magnetic resonance elastography (vMRE), were calculated and compared. Logistic regression analysis was performed to identify independent predictors of LVSI. The diagnostic performance of individual diffusion parameters and combined models incorporating significant clinical variables was evaluated. Internal validation was performed using 1,000 bootstrap resamples. Kaplan–Meier analysis was used to compare prognostic outcomes.

**Results:** Of the 113 patients, 45 were LVSI-positive and 68 were LVSI-negative. Among these diffusion models, the CTRW model achieved the highest AUC of 0.888 (accuracy : 0.850, AICc = 96.3). ADC , $\alpha_{CTRW}$ , and μDiff were identified as independent predictors of LVSI. Incorporating age ($P$ = 0.003) and menopausal status ($P$ = 0.005) yielded a combined model with an AUC of 0.910 (accuracy = 0.894, AICc = 100.2). Bootstrap-corrected AUCs were 0.893 and 0.892 for the imaging and combined models, respectively. Kaplan-Meier analysis demonstrated markedly shorter disease-free survival (DFS) in LVSI-positive patients (log-rank $P$ = 0.016).

**Conclusion:** ADC, $\alpha_{CTRW}$ and μDiff were independently associated with LVSI and provided complementary imaging information. Their combination showed promising performance for preoperative LVSI assessment, while LVSI positivity was associated with shorter disease-free survival.

**Keywords**

Endometrial carcinoma; multi-b-value DWI; lymphovascular space invasion; predictive performance; prognostic outcomes

## Introduction

Endometrial carcinoma (EC) is one of the most prevalent malignancies of the female genital tract, with a continuously rising incidence in recent years[1]. Lymphovascular space invasion (LVSI), defined as the presence of tumor cells within intra- or peritumoral lymphatic or vascular spaces[2], is an established independent risk factor for lymph node metastasis and a robust prognostic biomarker in EC patients. Patients with LVSI positivity suffer from elevated tumor recurrence rates and compromised long-term survival, thereby necessitating extended surgical resection, including para-aortic lymphadenectomy[3]. Accordingly, accurate preoperative identification of LVSI status is essential for individualized surgical planning and clinical risk stratification. Nevertheless, conventional magnetic resonance imaging (MRI) and endometrial biopsy fail to reliably detect LVSI, and definitive diagnosis still relies on postoperative histopathological examination of resected uterine specimens[4]. Given this clinical challenge, there is an urgent demand for noninvasive tools for the preoperative evaluation of LVSI in EC.

Recently, radiomics-based MRI models have been developed to facilitate the preoperative prediction of LVSI[5-7]. However, these analytical frameworks suffer from non-standardized workflows and limited biological interpretability of extracted radiomic features, substantially hindering their large-scale clinical translation and practical application[8]. Quantitative MRI techniques, including diffusion-weighted imaging (DWI) and magnetic resonance elastography (MRE), have emerged as

promising alternatives to overcome these limitations. Conventional monoexponential DWI is based on the assumption of unrestricted Gaussian water diffusion, which cannot adequately characterize the intricate microstructural heterogeneity of malignant lesions. Multiple non-Gaussian diffusion models derived from multi-b-value DWI, including diffusion kurtosis imaging (DKI)[9], intravoxel incoherent motion (IVIM)[10], stretched exponential model (SEM)[11], continuous-time random walk (CTRW)[12], and fractional-order calculus (FROC)[13], enable more comprehensive depiction of the tumor microenvironment and have demonstrated superior performance in characterizing pathological features across diverse solid malignancies. Several prior investigations have validated that several non-Gaussian models outperform the monoexponential model in the assessment of EC[14-16]. Nevertheless, their value for the preoperative prediction of LVSI remains insufficiently explored.

Additionally, tumor stiffness quantified by MRE is closely associated with invasive potential and disease progression[17]. Existing evidence has shown that MRE-derived stiffness metrics are independent predictors of LVSI positivity in EC[18], yet the technique demands dedicated hardware and specialized post-processing software, limiting its routine clinical deployment. Virtual MRE (vMRE), which can be obtained from multi-b-value DWI without additional specialized equipment, has demonstrated diagnostic performance comparable to that of conventional MRE[19]. To date, few studies have evaluated its predictive value for LVSI. Moreover, head-to-head comparisons across multiple non-Gaussian diffusion models for the preoperative LVSI assessment remain scarce, and the additional predictive value of integrating

multiparametric diffusion metrics with clinical variables has not been thoroughly characterized.

This study aimed to systematically compare 15 quantitative parameters derived from seven mathematical models of multi-b-value DWI for preoperative LVSI assessment in EC. We sought to identify independent imaging predictors through univariate analysis, collinearity assessment, and multivariable logistic regression, and to evaluate the performance of models based on the selected imaging and clinical variables. We also compared postoperative disease-free and overall survival between patients with and without LVSI.

## Materials and Methods

### Patients

The study protocol was approved by the Institutional Review Board. Written informed consent was waived for this retrospective analysis of collected preoperative imaging and pathological data. Consecutive women with suspected EC were recruited from November 2022 to April 2023 based on the following inclusion criteria: 1) preoperative pelvic MRI examinations, including conventional MRI and multi-b-value DWI, performed within 2 weeks before surgery; 2) patients who had undergone radical hysterectomy and pelvic lymph node dissection. The exclusion criteria were: 1) incomplete clinical and pathological data; 2) radiotherapy or chemotherapy before pelvic MRI; 3) no visible tumor or tumor with a maximum diameter of < 1 cm; 4) previous history of malignancy other than EC; 5) inadequate image quality for analysis (**Figure 1**). Finally, 113 patients were included in the study.

Clinical, laboratory and pathological data were extracted from the electronic medical database for subsequent analyses. Follow-up assessments were conducted every 3–6 months during the first 2 years after surgery and every 6 months thereafter. The final follow-up cutoff date was April 30, 2026. Disease-free survival (DFS) was defined as the time interval from surgery to the first documented tumor recurrence, distant metastasis, or all-cause death. Overall survival (OS) was defined as the time interval from surgery to death or the last follow-up visit. Patients lost to follow-up were censored at the date of their last documented follow-up.

**MRI acquisition**

All examinations were performed using a 3.0T MRI scanner (SIGNA™ Architect; GE HealthCare, Milwaukee, WI, USA) equipped with a 46-channel adaptive body receiver coil. All participants were examined during the non-menstrual phase and were required to fast for 4 hours beforehand to reduce bowel peristalsis and minimize motion artifacts. Additionally, patients were instructed to urinate and defecate 30 minutes prior to the examination to achieve moderate bladder filling. The imaging protocols included T2-weighted imaging, T1-weighted fluid-attenuated inversion recovery (FLAIR), T2-weighted FLAIR, contrast-enhanced T1-weighted imaging, and multi-b-value DWI. The acquisition parameters for multi-b-value DWI were: TR/TE = 3200/101 ms, FOV = 240×240 $mm^2$, matrix size = 128×128, slice thickness/gap = 5/0.5 mm, b-values = 0/10/20/50/100/200/400/800/1200/1500/2000/3000 $s/mm^2$.

**Image analysis**

Diffusion parametric maps of 7 diffusion models (DWI, DKI, IVIM, SEM, CTRW,

FROC, and vMRE) were calculated from multi-b-value DWI data using in-house MATLAB (MathWorks, Natick, MA, USA) scripts based on the combined-DWI-modeling codes (https://github.com/Arroway-JQ/combined-DWI-modeling-and-tumor-classification). Specifically, the diffusion models were defined as follows:

1. DWI model:

$$\frac{S_{(b)}}{S_0} = \exp(-b \times ADC)$$

where $S_b$ and $S_0$ represent the diffusion-weighted signal intensities acquired at b values of b (here we used only 800) and 0 s/mm$^2$, respectively, and ADC denotes the apparent diffusion coefficient.

2. DKI model:

$$\frac{S_{(b)}}{S_0} = \exp(-bD + \frac{b^2D^2K}{6})$$

where D and K represent mean diffusivity and mean kurtosis, respectively.

3. IVIM model:

$$\frac{S_{(b)}}{S_0} = (1 - f)\exp(-bD) + f \times \exp(-b \times D^*)$$

where D represents the pure diffusion coefficient, $D^*$ represents the pseudodiffusion coefficient of microcirculation, and f denotes the perfusion fraction.

4. SEM model:

$$\frac{S_{(b)}}{S_0} = \exp[-(bDDC)^{\alpha}]$$

where DDC represents the distributed diffusion coefficient, and α denotes the intravoxel diffusion heterogeneity index.

5. CTRW model:

$$\frac{S_{(b)}}{S_0} = E_\alpha\left[-(bD)^\beta\right]$$

where $E_\alpha$ represents the Mittag-Leffler function of α order, D represents the anomalous diffusion coefficient, and α and β denote the temporal and spatial diffusion heterogeneity, respectively.

6. FROC model:

$$\frac{S_{(b)}}{S_0} = \exp\left[-D\mu^{2(\beta-1)}(\gamma G_d \delta)^{2\beta}\left(\Delta - \frac{2\beta-1}{2\beta+1}\delta\right)\right]$$

where D represents anomalous diffusion coefficient, μ represents the spatial constant, and β represents the fractional-order derivative in space. Additionally, $G_d$ , δ, and Δ denote diffusion gradient amplitude, gradient pulse width, and gradient lobe separation, respectively.

7. vMRE:

$$\mu\text{Diff} = \alpha\ln[(S_{200}/S_{1500})/(1500-200)] + \beta$$

where μDiff represents the diffusion-based shear modulus, and $S_{200}$ and $S_{1500}$ denote diffusion-weighted signal intensities acquired at b values of 200 and 1500 s/mm$^2$, respectively. The α and β values are constants. μDiff represents the diffusion-based virtual shear modulus that reflects tissue stiffness and is reported in units of kPa. Le Bihan et al. described and summarized the quantification of stiffness values for vMRE. According to previous calibration studies performed in liver tissue, the constants α and β were set to −9.8±0.8 and 14±0.9, respectively[20].

Finally, 15 diffusion parameter maps were obtained, including ADC, MD, MK, D, $D^*$, f, $\alpha_{SEM}$, DDC, $\alpha_{CTRW}$, $\beta_{CTRW}$, $D_{CTRW}$, $\beta_{FROC}$, $D_{FROC}$, $\mu_{FROC}$, and μDiff. Subsequently, two radiologists (with 7 and 18 years of experience in abdominal imaging), who were

blinded to clinical and histopathological data, performed manual segmentation within ITK-SNAP 4.0 software. Three consecutive axial slices covering the largest tumor cross-section were selected on DWI images ($b = 800\ s/mm^2$), with T2-weighted and contrast-enhanced images as references. Cystic, necrotic, and hemorrhagic areas were carefully avoided during delineation. The software's image registration function was utilized to obtain the mean regions of interest (ROI) values for each parameter map.

**Statistical analysis**

GraphPad Prism (version 8.0) and R software (version 4.2.1) were used for statistical analyses. Interobserver agreement between two radiologists was evaluated using the intraclass correlation coefficient (ICC). ICC values exceeding 0.75 were considered to indicate good-to-excellent agreement. Normally distributed continuous variables were compared using the independent-sample t-test, whereas non-normally distributed continuous variables were compared using the Mann–Whitney U test. Categorical variables were compared using the chi-squared test. Variables with *P* < 0.05 in univariate analysis were included as candidates for multivariate analysis. Spearman's rank correlation coefficient was used to evaluate the correlations among candidate variables, with $|r| > 0.75$ considered to indicate strong correlation. Meanwhile, variance inflation factor (VIF) was employed to assess multicollinearity among variables, with VIF > 5 indicating significant multicollinearity. For variable groups exhibiting strong correlation or multicollinearity, the optimal representative variable was selected based on a comprehensive evaluation of clinical interpretability, univariate odds ratio (OR), and the area under the curve (AUC) of the univariate model, and then included in

subsequent analysis. Finally, independent predictive factors were identified through multivariate logistic regression. Receiver operating characteristic (ROC) curve analysis was performed to assess the diagnostic performance of individual and combined models for identifying LVSI in EC. The goodness of fit for multiple models was evaluated using the Corrected Akaike Information Criterion (AICc), and internally evaluated using a bootstrap resampling method (1000 bootstrap resamples). DeLong's test was used to compare the predictive performance of different models. Kaplan–Meier survival curves were generated to compare DFS and OS between the LVSI-positive and LVSI-negative groups. $P$ <0.05 was considered statistically significant.

# Results

## Clinicopathologic characteristics

A total of 113 patients were included in this study. LVSI was identified in 45 patients (39.8%), whereas the remaining 68 patients (60.2%) demonstrated no evidence of LVSI on final histopathological examination. Clinical and pathological characteristics of the eligible patients are summarized in **Table 1**. The mean age was 55.84 ± 11.15 years in the LVSI-positive group and 48.21 ± 11.30 years in the LVSI-negative group, with a significant intergroup difference ($P$ = 0.003). The proportion of postmenopausal patients in the LVSI-positive group was significantly higher than that in the LVSI-negative group ($P$ = 0.005). No significant differences were observed between two groups in terms of irregular vaginal bleeding ($P$ = 0.562), hypertension ($P$ = 0.604), diabetes mellitus ($P$ = 0.838), body mass index (BMI; $P$ = 0.543), cancer antigen 125

(CA125; $P = 0.911$), or CA199 ($P = 0.420$).

**Analysis of diffusion parameters**

The ICCs for the diffusion parameters ranged from 0.825 to 0.963 (**Table S1**), indicating a good interobserver consistency across all parameters. Comparisons of diffusion parameters between LVSI-positive and LVSI-negative groups are presented in **Table 2** and **Figure 2**. Fourteen variables with $P < 0.05$ in univariate logistic regression were selected as candidates for multivariate analysis. Spearman's rank correlation coefficient and VIF were applied for multicollinearity assessment. Four diffusion-derived parameters ($D_{CTRW}$, $D_{FROC}$, MD, DDC) showed strong inter-correlations with VIF values all greater than 5, indicating significant multicollinearity. MD was chosen as the representative variable of this group based on comprehensive evaluation of clinical interpretability, univariate OR values and univariate-model AUC, while the other three collinear parameters were excluded. After collinearity screening, a total of 11 candidate variables were subjected to multivariate logistic regression analysis, ADC, $\alpha_{CTRW}$, and μDiff as independent predictors of LVSI in EC (**Table 3**), with VIF values of 2.092, 1.861 and 1.588, respectively, indicating no significant multicollinearity among these predictors. Representative cases are shown in **Figure 3 and 4** .

**Predictive performance**

The results of ROC analyses for diffusion and clinical parameters that differed significantly between two groups are presented in **Table 4** and **Figure 5**. For the diffusion models, the AUC, accuracy, sensitivity, and specificity for differentiating

LVSI-positive from LVSI-negative EC ranged from 0.773 to 0.888, 0.770 to 0.850, 0.763 to 0.822, and 0.721 to 0.885, respectively. Among these models, the CTRW model achieved the highest AUC of 0.888 (accuracy : 0.850, AICc = 96.3). The model constructed with three independent imaging predictors obtained an AUC of 0.904 (accuracy = 0.885, AICc = 100.9). After further incorporating two clinical variables (age and menopausal status), the combined model achieved an AUC of 0.910 (accuracy = 0.894, AICc = 100.2). Although the combined model had a higher AICc than the CTRW model (100.2 vs. 96.3), it showed improved discrimination and classification performance, with higher AUC, accuracy, sensitivity, and specificity. Internal validation using 1,000 bootstrap resamples yielded optimism-corrected AUCs of 0.893 and 0.892 for the imaging and combined models, respectively, indicating that their discriminative performance remained robust after correction for optimism. In addition, the DeLong test demonstrated statistically significant differences between the combined model and the individual diffusion models ( $P < 0.05$).

**Prognostic outcomes**

Kaplan-Meier analysis revealed that patients with LVSI-positive status had significantly shorter DFS than those with LVSI-negative disease (log-rank $P = 0.016$). However, no significant difference in OS was observed between two groups (log-rank $P = 0.679$; **Figure 6**). Univariate Cox regression analysis further demonstrated that LVSI positivity was associated with poorer DFS (HR = 3.45, 95% CI: 1.18–10.10, $P = 0.024$), whereas LVSI status was not significantly associated with OS (HR = 1.51, 95% CI: 0.21–10.71, $P = 0.681$). Numbers at risk in each group are displayed below the

horizontal axis in **Figure 6**.

## Discussion

This study evaluated 7 diffusion models derived from multi-b-value DWI, comprising 15 quantitative parameters, and systematically compared their performance for identifying LVSI in EC. ADC, $\alpha_{CTRW}$, and μDiff were identified as independent LVSI predictors, and the three-parameter imaging model yielded an AUC of 0.904. Incorporating clinical variables of age and menopausal status further elevated the AUC of the combined clinical–imaging model to 0.910. Survival analysis further revealed that LVSI-positive patients carried higher risks of disease recurrence and distant metastasis, highlighting the clinical importance of accurate preoperative LVSI risk stratification.

Among the clinical characteristics evaluated, age and menopausal status differed significantly between LVSI-positive and LVSI-negative groups. Age-related biological alterations may be partly ascribed to the upregulation of proapoptotic and inflammatory cytokines, alongside impaired systemic immune function in elderly individuals. Atrophic endometrium develops in the majority of women within 5 years after menopause[21]. Longer postmenopausal duration correlates with an increased overall risk of EC and a higher proportion of poorly differentiated tumors and special histological subtypes[22]. Previous cohort studies have verified that EC in older and postmenopausal patients tends to exhibit more aggressive biological behavior. Dysregulated endogenous hormonal homeostasis may induce aberrant angiogenesis and

lymphangiogenesis, thereby promoting the migration and invasion of neoplastic cells[23]. Age and menopausal status have also been identified as independent predictors for discriminating endometrial hyperplasia from malignant endometrial lesions[16, 24]. Nevertheless, our present study demonstrated that clinical variables alone had limited diagnostic performance for preoperative detection of LVSI and were insufficient to satisfy clinical requirements for accurate risk prediction.

Multivariate regression analysis confirmed three reliable imaging biomarkers for the preoperative prediction of LVSI. As the most fundamental diffusion parameter, ADC quantitatively reflects the degree of free water motion within tumour tissues, with its numerical values highly sensitive to alterations in cellular microstructure and interstitial microenvironment. Decreased ADC is predominantly attributed to excessive tumour proliferation, dense cellular arrangement and narrowed extracellular interstitial spaces, which synergistically exacerbate intracellular water diffusion restriction. This classic imaging-pathological correspondence has been fully validated in previous investigations of EC microscopic features[25, 26]. As a core temporal heterogeneity parameter derived from CTRW model, $\alpha_{CTRW}$ enables quantitative evaluation of time-dependent variations in water molecular motion within structurally heterogeneous tumour microenvironments[27]. Lower $\alpha_{CTRW}$ values in LVSI-positive tumours indicate restricted diffusion behaviour with a temporally stabilized pattern, which represents a typical signature of disordered cell-cycle progression and homogeneous proliferative activity in invasive lesions. Capable of capturing subtle microstructural tumoral aberrations undetectable by conventional ADC, $\alpha_{CTRW}$ provides supplementary

predictive information for invasive pathological phenotypes and compensates for the inherent diagnostic limitations of traditional diffusion parameters[28]. Notably, this advanced CTRW-derived biomarker remains insufficiently investigated in preoperative LVSI risk stratification for EC.

In addition to conventional diffusion biomarkers, our study further demonstrated that μDiff serves as an independent predictive factor for LVSI. Stiffness parameters derived from conventional MRE have been identified as independent predictors of LVSI in prior literature[18]. Elevated μDiff values in LVSI-positive lesions stem from comprehensive tumoral microstructural remodelling, including extensive LVSI, interstitial collagen deposition, and densely compacted tumour cellular architecture. These pathological alterations collectively increase tissue rigidity and interstitial diffusion resistance, ultimately leading to higher quantitative μDiff measurements. Tumour microenvironment stiffening is biologically coupled with enhanced cellular invasion and migration capabilities, providing a solid biophysical mechanism underlying the close correlation between elevated tissue stiffness and adverse LVSI status in endometrial carcinoma. From a methodological perspective, vMRE enables non-invasive quantitative stiffness assessment exclusively based on routine multi-b-value DWI datasets, eliminating the need for specialized hardware and additional scanning sequences required for conventional mechanical MRE. Such technical superiority grants vMRE excellent clinical accessibility and promising translational prospects for standardized preoperative risk stratification in routine clinical practice.

With the exception of D*, all remaining parameters showed statistically significant

inter-group differences in univariate analysis. These differential alterations reflect comprehensive microstructural and microvascular remodelling occurring in LVSI-positive endometrial lesions. As a core quantitative metric of diffusion kurtosis imaging, MK sensitively characterizes non-Gaussian water diffusion patterns induced by excessive cellular proliferation and disorganized tissue architecture in high-risk endometrial tumours. This finding is consistent with previous evidence demonstrating that elevated kurtosis values are closely correlated with aggressive pathological phenotypes in EC[14]. Similarly, IVIM-based pure diffusion and perfusion parameters revealed distinct intratumoral microcirculatory disparities between LVSI-positive and LVSI-negative cases, further supporting the notion that impaired microperfusion and restricted water diffusion are tightly associated with increased invasive potential of endometrial malignancy[29]. Parameters derived from CTRW, FROC, and SEM models provide refined microstructural information that conventional monoexponential ADC cannot fully resolve, enabling comprehensive characterization of layered tissue heterogeneity, disordered molecular transport kinetics, and continuous microscopic diffusion gradients. Such multi-model diffusion signatures have been validated as effective biomarkers for evaluating tumour aggressiveness across various malignant tumours[30-32]. Although these biologically meaningful imaging alterations were prominent in univariate comparisons, they failed to retain independent predictive capacity after comprehensive multivariate adjustment. This phenomenon is biologically reasonable, as the microstructural and microvascular variations captured by these secondary parameters essentially represent downstream phenotypic manifestations of

core pathological alterations, including increased cellular density and tumour microenvironment stiffening, which are predominantly quantified by ADC, $\alpha_{CTRW}$, and μDiff. Consequently, these secondary diffusion metrics reflect overlapping tumour biological characteristics and lack independent predictive dimensions, explaining their attenuated diagnostic performance in the integrated clinical-radiological multivariate model.

The combined model integrating clinical indicators with ADC, $\alpha_{CTRW}$, and μDiff achieved an AUC of 0.910 for predicting LVSI. The three parameters may provide complementary descriptions of water mobility, diffusion heterogeneity, and tissue stiffness. After internal validation using 1,000 bootstrap resamples, the optimism-corrected AUCs were 0.893 for the imaging model and 0.892 for the combined model. Notably, although the addition of age and menopausal status slightly improved the apparent discriminative performance, this improvement was not maintained after bootstrap correction, suggesting that the incremental predictive value of these clinical variables may be limited in the present cohort. Nevertheless, the predictive performance comparable to recently reported radiomics models for LVSI assessment in EC[5-7]. Unlike high-dimensional radiomics approaches that require cumbersome feature extraction and selection procedures, our model relies on easily accessible quantitative parameters derived directly from multi-b-value DWI, thereby simplifying post-processing and potentially facilitating clinical translation. In our survival analyses, LVSI-positive patients demonstrated significantly impaired disease-free survival, while no statistically significant between-group difference was observed for overall survival.

This discrepancy is most plausibly explained by the relatively limited follow-up duration in our cohort; differences in late recurrence and long-term overall survival may manifest with prolonged observational periods. These survival findings underscore the clinical necessity of pre-operative LVSI risk stratification to guide individualized surgical and adjuvant therapeutic decision-making.

This study had several limitations. First, it was a single-center retrospective analysis with a moderate sample size, which may have introduced selection bias and limited the external generalizability of the predictive model. Multicenter prospective studies are therefore needed to validate its robustness. Second, only preoperative quantitative parameters derived from static DWI acquisitions were analyzed. Longitudinal changes in these parameters during adjuvant therapy and long-term follow-up were not assessed, restricting our understanding of dynamic tumor microenvironment evolution. Third, the vMRE parameters are derived from liver tissue, and their applicability to uterine tissue requires repeated validation. Future studies should perform recalibration and explore the biological significance of μDiff. Finally, the follow-up duration for survival endpoint observation was relatively short. Although a significant intergroup difference in DFS was observed, long-term OS disparities and late distant metastasis events need continuous long-term follow-up data for further confirmation.

In conclusion, systematic comparison of parameters calculated from multi-b-value DWI identified ADC, $\alpha_{CTRW}$, and μDiff as independent imaging predictors of LVSI in EC. These statistically selected parameters may provide complementary information on water mobility, diffusion heterogeneity, and tissue stiffness, and their combination

showed promising performance for preoperative LVSI assessment. Multi-b-value DWI may therefore offer a unified quantitative approach for characterizing the LVSI-associated tumor microenvironment.

**Funding**

This work was supported by Shandong Provincial Medical Association (YXH2024YS032) and Natural Science Foundation of Shandong Province (ZR2026QC2157Z).

**Declarations**

**Competing interests** The authors declare no competing interests.

1. Ferrari, F. and A. Giannini, *Approaches to prevention of gynecological malignancies*. Bmc Womens Health, 2024. **24**(1).DOI:10.1186/s12905-024-03100-4
2. Matias-Guiu, X., C.I. Selinger, L. Anderson, et al., *Data Set for the Reporting of Endometrial Cancer: Recommendations From the International Collaboration on Cancer Reporting (ICCR).* International Journal of Gynecological Pathology, 2022. **41**: p. S90-S118.DOI:10.1097/pgp.0000000000000901
3. Briët, J.M., H. Hollema, N. Reesink, et al., *Lymphvascular space involvement: an independent prognostic factor in endometrial cancer.* Gynecologic Oncology, 2005. **96**(3): p. 799-804.DOI:10.1016/j.ygyno.2004.11.033
4. Braun, M.M., E.A. Overbeek-Wager and R.J. Grumbo, *Diagnosis and Management of Endometrial Cancer.* American Family Physician, 2016. **93**(6): p. 468-474
5. Liu, D., J.Y. Huang, Y.F. Zhang, et al., *Multimodal MRI-based radiomics models for the preoperative prediction of lymphovascular space invasion of endometrial carcinoma.* Bmc Medical Imaging, 2024. **24**(1).DOI:10.1186/s12880-024-01430-1
6. Wang, J.J., X.H. Zhang, X.H. Guo, et al., *Prediction of Lymphovascular Space Invision in Endometrial Cancer based on Multi-parameter MRI Radiomics Model.* Current Medical Imaging, 2024. **20**.DOI:10.2174/0115734056266366231219111246
7. Yi, Q.Q., Y. Wang, S.S. Zou, et al., *A comprehensive magnetic resonance imaging-based model for predicting lymphovascular space invasion in endometrial cancer: a retrospective observational study.* Quantitative Imaging in Medicine and Surgery, 2025. **15**(12).DOI:10.21037/qims-2025-1031

8. Bi, W.L., A. Hosny, M.B. Schabath, et al., *Artificial intelligence in cancer imaging: Clinical challenges and applications.* Ca-a Cancer Journal for Clinicians, 2019. **69**(2): p. 127-157.DOI:10.3322/caac.21552
9. Jensen, J.H., J.A. Helpern, A. Ramani, H.Z. Lu and K. Kaczynski, *Diffusional kurtosis imaging: The quantification of non-Gaussian water diffusion by means of magnetic resonance imaging.* Magnetic Resonance in Medicine, 2005. **53**(6): p. 1432-1440.DOI:10.1002/mrm.20508
10. Iima, M. and D. Le Bihan, *Clinical Intravoxel Incoherent Motion and Diffusion MR Imaging: Past, Present, and Future.* Radiology, 2016. **278**(1): p. 13-32.DOI:10.1148/radiol.2015150244
11. Bennett, K.M., K.M. Schmainda, R. Bennett, D.B. Rowe, H.B. Lu and J.S. Hyde, *Characterization of continuously distributed cortical water diffusion rates with a stretched-exponential model.* Magnetic Resonance in Medicine, 2003. **50**(4): p. 727-734.DOI:10.1002/mrm.10581
12. Karaman, M.M., Y. Sui, H. Wang, R.L. Magin, Y.H. Li and X.J. Zhou, *Differentiating Low- and High-Grade Pediatric Brain Tumors Using a Continuous-Time Random-Walk Diffusion Model at High b-Values.* Magnetic Resonance in Medicine, 2016. **76**(4): p. 1149-1157.DOI:10.1002/mrm.26012
13. Tang, L., Y. Sui, Z. Zhong, et al., *Non-Gaussian diffusion imaging with a fractional order calculus model to predict response of gastrointestinal stromal tumor to second-line sunitinib therapy.* Magnetic Resonance in Medicine, 2018. **79**(3): p. 1399-1406.DOI:10.1002/mrm.26798
14. Zhang, G.Y., R.F. Yan, W.Y. Liu, et al., *Use of biexponential and stretched exponential models of intravoxel incoherent motion and dynamic contrast-enhanced magnetic resonance imaging to assess the proliferation of endometrial carcinoma.* Quantitative Imaging in Medicine and Surgery, 2023. **13**(4): p. 2568-2581.DOI:10.21037/qims-22-688
15. Zhang, Q., H. Ouyang, F. Ye, et al., *Multiple mathematical models of diffusion-weighted imaging for endometrial cancer characterization: Correlation with prognosis-related risk factors.* European Journal of Radiology, 2020. **130**.DOI:10.1016/j.ejrad.2020.109102
16. Bi, Q., Y.C. Deng, N. Xu, et al., *Differentiation of early-stage endometrial carcinoma from benign endometrial lesions: a comparative study of six diffusion models.* Quantitative Imaging in Medicine and Surgery, 2025. **15**(1).DOI:10.21037/qims-24-896
17. Zhang, L.Q., X. Long, M. Nijiati, et al., *Tumor stiffness measured by 3D magnetic resonance elastography can help predict the aggressiveness of endometrial carcinoma: preliminary findings.* Cancer Imaging, 2021. **21**(1).DOI:10.1186/s40644-021-00420-8
18. Long, L., M.L. Liu, X.J. Deng, et al., *Tumor Stiffness Measurement at Multifrequency MR Elastography to Predict Lymphovascular Space Invasion in Endometrial Cancer.* Radiology, 2024. **311**(3).DOI:10.1148/radiol.232242
19. Kromrey, M.L., D. Le Bihan, S. Ichikawa and U. Motosugi, *Diffusion-weighted MRI-based Virtual Elastography for the Assessment of Liver Fibrosis.* Radiology, 2020. **295**(1): p. 127-135.DOI:10.1148/radiol.2020191498
20. Le Bihan, D., S. Ichikawa and U. Motosugi, *Diffusion and Intravoxel Incoherent Motion MR Imaging-based Virtual Elastography: A Hypothesis-generating Study in the Liver.*

Radiology, 2017. **285**(2): p. 609-619.DOI:10.1148/radiol.2017170025
21. Papakonstantinou, E. and G. Adonakis, *Management of pre-, peri-, and post-menopausal abnormal uterine bleeding: When to perform endometrial sampling?* International Journal of Gynecology & Obstetrics, 2022. **158**(2): p. 252-259.DOI:10.1002/ijgo.13988
22. Lee, Y.L., Y.S. Bai and C.S. Yin, *Vaginoscopic hysteroscopy in management for women with post-menopausal vaginal bleeding.* Taiwanese Journal of Obstetrics & Gynecology, 2019. **58**(4): p. 497-500.DOI:10.1016/j.tjog.2019.05.012
23. Kuai, D., Q.T. Tang, W.Y. Tian and H.Y. Zhang, *Rapid identification of endometrial hyperplasia and endometrial endometrioid cancer in young women.* Discover Oncology, 2023. **14**(1).DOI:10.1007/s12672-023-00736-w
24. Su, J., L.N. She, Y. Fan, et al., *Model Predicting the Risk of Endometrial Hyperplasia Developing into Endometrial Cancer.* Journal of Inflammation Research, 2024. **17**: p. 6159-6171.DOI:10.2147/jir.S471620
25. Ma, X.L., X.J. Ren, M.H. Shen, et al., *Volumetric ADC histogram analysis for preoperative evaluation of LVSI status in stage I endometrioid adenocarcinoma.* European Radiology, 2022. **32**(1): p. 460-469.DOI:10.1007/s00330-021-07996-6
26. Jin, X.X., R.F. Yan, Z. Li, et al., *Evaluation of Amide Proton Transfer-Weighted Imaging for Risk Factors in Stage I Endometrial Cancer: A Comparison With Diffusion-Weighted Imaging and Diffusion Kurtosis Imaging.* Frontiers in Oncology, 2022. **12**.DOI:10.3389/fonc.2022.876120
27. Hua, L., Q.Y. Guo, Y.F. Tang, et al., *Using non-Gaussian diffusion models to distinguish benign from malignant head and neck lesions.* Frontiers in Oncology, 2025. **15**.DOI:10.3389/fonc.2025.1581637
28. Li, W.E., Y.L. Jiang, J. Ai, Q. Miao, C.B. Li and R.M. Chai, *Non-Gaussian diffusion MRI models for preoperative assessment of microvascular invasion in hepatocellular carcinoma.* Abdominal Radiology, 2026. **51**(3): p. 1312-1324.DOI:10.1007/s00261-025-05113-5
29. Satta, S., M. Dolciami, V. Celli, et al., *Quantitative diffusion and perfusion MRI in the evaluation of endometrial cancer: validation with histopathological parameters.* British Journal of Radiology, 2021. **94**(1125).DOI:10.1259/bjr.20210054
30. Zhang, H., Y.Y. Zhou, J. Li, P.J. Zhang, Z.Z. Li and J.W. Guo, *The value of DWI in predicting the response to synchronous radiochemotherapy for advanced cervical carcinoma: comparison among three mathematical models.* Cancer Imaging, 2020. **20**(1).DOI:10.1186/s40644-019-0285-6
31. Li, H.X., L.L. Wang, J. Zhang, Q. Duan, Y.K. Xu and Y.J. Xue, *Evaluation of microvascular invasion of hepatocellular carcinoma using whole-lesion histogram analysis with the stretched-exponential diffusion model.* British Journal of Radiology, 2022. **95**(1132).DOI:10.1259/bjr.20210631
32. He, L.T., F. Li, Y.J. Qin, et al., *Enhanced preoperative prediction of breast lesion pathology, prognostic biomarkers, and molecular subtypes using multiple models diffusion-weighted MR imaging.* Scientific Reports, 2025. **15**(1).DOI:10.1038/s41598-024-81713-3

**Figure 1 Flow diagram of patient inclusion and exclusion criteria**

**Figure 2 Boxplots of diffusion parameters in LVSI-positive group and LVSI-negative group.**

**Figure 3 DWI and multi-b-value DWI-derived images of a 67-year-old female with LVSI-positive uterine serous carcinoma.**

**Figure 4 DWI and multi-b-value DWI-derived images of a 61-year-old female with LVSI-negative endometrioid adenocarcinoma.**

**Figure 5 Receiver operating characteristic curves for differentiating LVSI-positive group and LVSI-negative group.**

**Figure 6 Kaplan-Meier curve for disease-free survival and overall survival LVSI-positive group and LVSI-negative group.**

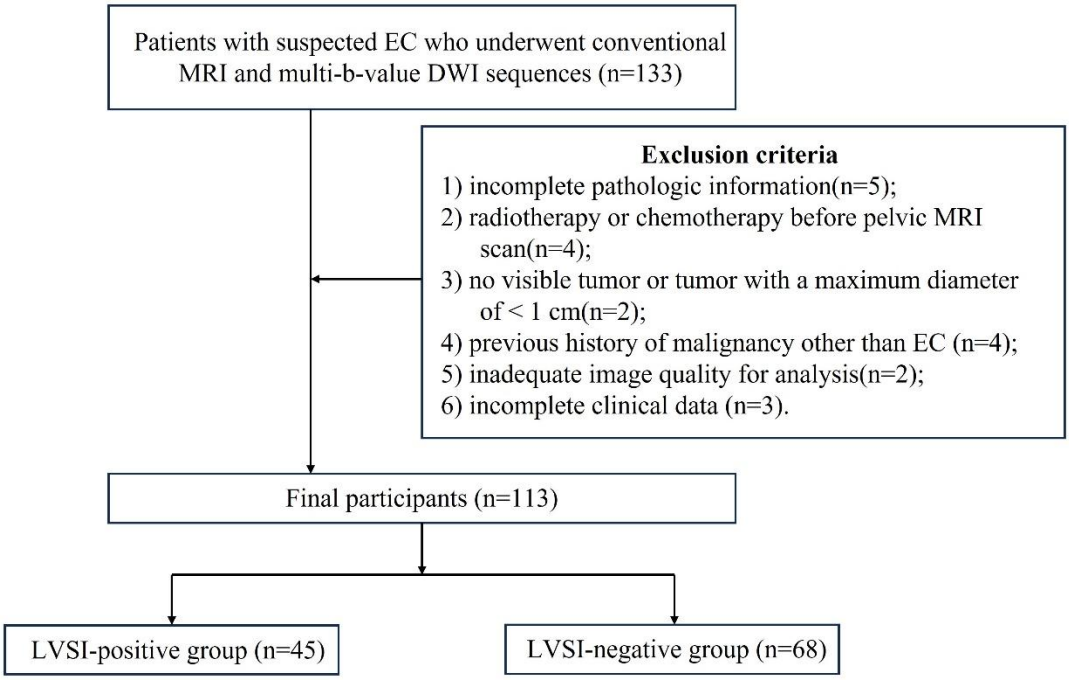



**Figure 1 Flow diagram of patient inclusion and exclusion criteria**

**Table 1 Comparison of characteristics between the LVSI-positive group and LVSI-negative group**

| Characteristic | LVSI-positive group (n = 45) | LVSI-negative group (n = 68) | *P* value |
|---|---|---|---|
| Age (years) | 55.84 ± 11.15 | 48.21 ± 11.30 | 0.003 |
| BMI (kg/m$^2$) | 25.71 (4.67) | 27.09 (4.91) | 0.316 |
| Menopause (yes/no), n (%) | 35 (77.8)/10 (22.2) | 35 (51.5)/33 (48.5) | 0.005 |
| Irregular vaginal bleeding | 34 (75.6)/11 (24.4) | 48 (70.6)/20 (29.4) | 0.562 |
| Hypertension (yes/no), n (%) | 16 (35.6)/29 (64.4) | 21 (30.9)/47 (69.1) | 0.604 |
| Diabetes (yes/no), n (%) | 6 (13.3)/39 (86.7) | 10 (14.7)/58 (85.3) | 0.838 |
| CA125 (U/mL) | 16.96 (35.91) | 17.94 (16.99) | 0.911 |
| CA199 (U/mL) | 25.57 (41.64) | 25.67 (39.42) | 0.420 |
| Histological type, n (%) | | | 0.272 |
| EA | 38 (84.4) | 62 (91.2) | |
| Non-EA | 7 (15.6) | 6 (8.8) | |

Continuous variables for normal and skew distributions are presented as mean ± standard deviation and as median (interquartile range), respectively. Interquartile range = percentiles 75 – percentiles 25. Categorical variables are described as number of observations and percentages in parentheses. BMI, body mass index; CA, cancer antigen; EA, Endometrioid adenocarcinoma

**Table 2 Comparison of diffusion parameters Between LVSI-positive group and LVSI-negative group**

| Model | Parameters | LVSI-positive group | LVSI-negative group | *P* value |
|---|---|---|---|---|
| DWI | ADC ($10^{-3}$ mm$^2$/s) | 0.808 (0.100) | 0.916 (0.080) | < 0.001 |
| CTRW | $\alpha_{CTRW}$ | 0.816 (0.100) | 0.914 (0.100) | < 0.001 |
| | $\beta_{CTRW}$ | 0.748 ± 0.078 | 0.808 (0.090) | 0.001 |
| | $D_{CTRW}$ ($10^{-3}$ mm$^2$/s) | 0.804 ± 0.047 | 0.847 ± 0.039 | < 0.001 |
| FROC | $\beta_{FROC}$ | 0.773 ± 0.086 | 0.848 (0.080) | < 0.001 |
| | $\mu_{FROC}$ (mm) | 2.952 ± 0.213 | 2.755 ± 0.195 | < 0.001 |
| | $D_{FROC}$ ($10^{-3}$ mm$^2$/s) | 0.838 (0.080) | 0.889 (0.070) | < 0.001 |
| DKI | MD ($10^{-3}$ mm$^2$/s) | 0.855 (0.090) | 0.932 (0.100) | < 0.001 |
| | MK | 0.922 (0.090) | 0.835 (0.060) | < 0.001 |
| IVIM | D ($10^{-3}$ mm$^2$/s) | 9.423 (2.270) | 12.694 (4.830) | < 0.001 |
| | D* ($10^{-3}$ mm$^2$/s) | 0.459 ± 0.055 | 0.475 (0.070) | 0.067 |
| | f (%) | 0.339 ± 0.061 | 0.362 (0.080) | 0.015 |
| SEM | $\alpha_{SEM}$ | 0.627 ± 0.059 | 0.685 (0.080) | < 0.001 |
| | DDC ($10^{-3}$ mm$^2$/s) | 0.847 ± 0.100 | 0.927 (0.110) | < 0.001 |
| vMRE | μDiff (kPa) | 7.688 ± 0.984 | 6.556 ± 0.812 | < 0.001 |

Continuous variables for normal and skew distributions are presented as mean ± standard deviation and as median (interquartile range), respectively. Interquartile range = percentiles 75 – percentiles 25. DWI, diffusion-weighted imaging; ADC, apparent diffusion coefficient; CTRW, continuous-time random walk; $\alpha_{CTRW}$, temporal diffusion heterogeneity index; $\beta_{CTRW}$, spatial diffusion heterogeneity index; $D_{CTRW}$, anomalous diffusion coefficient; FROC, fractional order calculus; $\beta_{FROC}$, fractional order derivative in space; $\mu_{FROC}$, spatial constant; $D_{FROC}$, diffusion coefficient. DKI, diffusion kurtosis imaging; MD, mean diffusivity; MK, mean kurtosis; D, true diffusion coefficient; D*, pseudodiffusion coefficient; f, perfusion fraction; SEM, stretched exponential model; $\alpha_{SEM}$, intravoxel diffusion heterogeneity index; DDC, distributed diffusion coefficient; vMRE, virtual MR elastography.

**Table 3 Univariate and multivariate analyses for identifying LVSI-positive group and LVSI-negative group**

| Model | Parameters | Univariate analyses | | Multivariate analyses | |
|---|---|---|---|---|---|
| | | OR (95% CI) | *P* value | OR (95% CI) | *P* value |
| DWI | ADC ($10^{-3}$ $mm^2/s$) | 0.820 (0.741,0.903) | < 0.001 | 0.861 (0.783,0.947) | 0.002 |
| CTRW | $\alpha_{CTRW}$ | 0.851 (0.772,0.938) | < 0.001 | 0.883 (0.799,0.976) | 0.014 |
| | $\beta_{CTRW}$ | 0.812 (0.675,0.976) | 0.026 | 0.832 (0.673,1.081) | 0.134 |
| FROC | $\beta_{FROC}$ | 0.892 (0.793,0.944) | 0.006 | 0.907 (0.760,1.089) | 0.283 |
| | $\mu_{FROC}$ (mm) | 1.008 (0.997,1.018) | 0.097 | | |
| DKI | MD ($10^{-3}$ $mm^2/s$) | 0.817 (0.743,0.907) | < 0.001 | 0.906 (0.782,1.050) | 0.189 |
| | MK | 2.014 (1.432,4.016) | < 0.001 | 2.118 (0.929,4.828) | 0.074 |
| IVIM | D ($10^{-3}$ $mm^2/s$) | 0.882 (0.803,0.969) | 0.009 | 0.932 (0.851,1.021) | 0.130 |
| | f (%) | 0.902 (0.796,1.022) | 0.107 | | |
| SEM | $\alpha_{SEM}$ | 0.892 (0.787,0.989) | 0.031 | 0.954 (0.911,1.126) | 0.382 |

| | | | | | |
|---|---|---|---|---|---|
| vMRE | μDiff (kPa) | 4.219 (1.907,9.121) | < 0.001 | 3.024 (1.186,7.754) | 0.022 |

All factors with $p<0.05$ in univariate analyses were included in multivariate regression analyses. Values in bold indicate the logistic regression analyses with statistical significance. OR: odds ratio; CI: confidence interval; DWI, diffusion-weighted imaging; ADC, apparent diffusion coefficient; CTRW, continuous-time random walk; $\alpha_{CTRW}$, temporal diffusion heterogeneity index; $\beta_{CTRW}$, spatial diffusion heterogeneity index; FROC, fractional order calculus; $\beta_{FROC}$, fractional order derivative in space; $\mu_{FROC}$, spatial constant; DKI, diffusion kurtosis imaging; MD, mean diffusivity; MK, mean kurtosis; D, true diffusion coefficient; D*, pseudodiffusion coefficient; f, perfusion fraction; SEM, stretched exponential model; $\alpha_{SEM}$, intravoxel diffusion heterogeneity index; vMRE, virtual MR elastography.

**Table 4 Diagnostic Performance of diffusion parameters Between LVSI-positive group and LVSI-negative group**

| | AUC | 95% CI | Cut-off* | Accuracy | Sensitivity | Specificity | AICc |
|---|---|---|---|---|---|---|---|
| ADC ($10^{-3}$ $mm^2/s$) | 0.851 | 0.772 to 0.929 | 0.853 | 0.814 | 0.819 | 0.824 | 111.9 |
| $\alpha_{CTRW}$ | 0.842 | 0.763 to 0.922 | 0.871 | 0.788 | 0.837 | 0.794 | |
| $\beta_{CTRW}$ | 0.732 | 0.631 to 0.832 | 0.788 | 0.726 | 0.778 | 0.662 | |
| $D_{CTRW}$ ($10^{-3}$ $mm^2/s$) | 0.756 | 0.662 to 0.849 | 0.809 | 0.743 | 0.656 | 0.828 | |
| $\beta_{FROC}$ | 0.703 | 0.602 to 0.805 | 0.825 | 0.681 | 0.756 | 0.676 | |
| $\mu_{FROC}$ (mm) | 0.755 | 0.663 to 0.846 | 2.895 | 0.690 | 0.644 | 0.694 | |
| $D_{FROC}$ ($10^{-3}$ $mm^2/s$) | 0.715 | 0.615 to 0.815 | 0.866 | 0.708 | 0.778 | 0.691 | |
| MD ($10^{-3}$ $mm^2/s$) | 0.747 | 0.652 to 0.842 | 0.908 | 0.726 | 0.827 | 0.629 | |
| MK | 0.809 | 0.724 to 0.894 | 0.852 | 0.770 | 0.844 | 0.721 | |
| D ($10^{-3}$ $mm^2/s$) | 0.739 | 0.639 to 0.839 | 9.967 | 0.717 | 0.689 | 0.838 | |
| f (%) | 0.693 | 0.591 to 0.796 | 0.327 | 0.673 | 0.511 | 0.812 | |
| $\alpha_{SEM}$ | 0.749 | 0.656 to 0.842 | 0.660 | 0.752 | 0.756 | 0.750 | |
| DDC ($10^{-3}$ $mm^2/s$) | 0.744 | 0.649 to 0.839 | 0.886 | 0.752 | 0.777 | 0.750 | |
| μDiff (kPa) | 0.830 | 0.748 to 0.911 | 7.305 | 0.796 | 0.756 | 0.809 | |
| Age (years) | 0.669 | 0.570 to 0.769 | 54.500 | 0.628 | 0.800 | 0.715 | |

| | | | | | | | |
|---|---|---|---|---|---|---|---|
| Menopausal status | 0.646 | 0.544 to 0.749 | 0.500 | 0.602 | 0.778 | 0.575 | |
| CTRW | 0.888 | 0.824 to 0.948 | 0.484 | 0.850 | 0.811 | 0.885 | 96.3 |
| FROC | 0.864 | 0.794 to 0.935 | 0.417 | 0.814 | 0.822 | 0.794 | 110.3 |
| DKI | 0.829 | 0.749 to 0.910 | 0.404 | 0.796 | 0.802 | 0.779 | 128.9 |
| IVIM | 0.773 | 0.684 to 0.861 | 0.415 | 0.770 | 0.778 | 0.721 | 135.7 |
| SEM | 0.831 | 0.754 to 0.907 | 0.463 | 0.805 | 0.763 | 0.824 | 122.8 |
| ADC+$\alpha_{CTRW}$ +μDiff | 0.904 | 0.849 to 0.967 | 0.403 | 0.885 | 0.844 | 0.891 | 100.9 |
| Age + Menopausal status +ADC+$\alpha_{CTRW}$ +μDiff | 0.910 | 0.850 to 0.969 | 0.411 | 0.894 | 0.854 | 0.892 | 100.2 |

*The cutoff value was determined using Youden index. AUC: Area Under the Curve; CI: confidence interval; AICc :Akaike Information Criterion; DWI, diffusion-weighted imaging; ADC, apparent diffusion coefficient; CTRW, continuous-time random walk; $\alpha_{CTRW}$, temporal diffusion heterogeneity index; $\beta_{CTRW}$, spatial diffusion heterogeneity index; $D_{CTRW}$, anomalous diffusion coefficient; FROC, fractional order calculus; $\beta_{FROC}$, fractional order derivative in space; $\mu_{FROC}$, spatial constant; $D_{FROC}$, diffusion coefficient. DKI, diffusion kurtosis imaging; MD, mean diffusivity; MK, mean kurtosis; D, true diffusion coefficient; f, perfusion fraction; SEM, stretched exponential model; $\alpha_{SEM}$, intravoxel diffusion heterogeneity index; DDC, distributed diffusion coefficient; vMRE, virtual MR elastography.

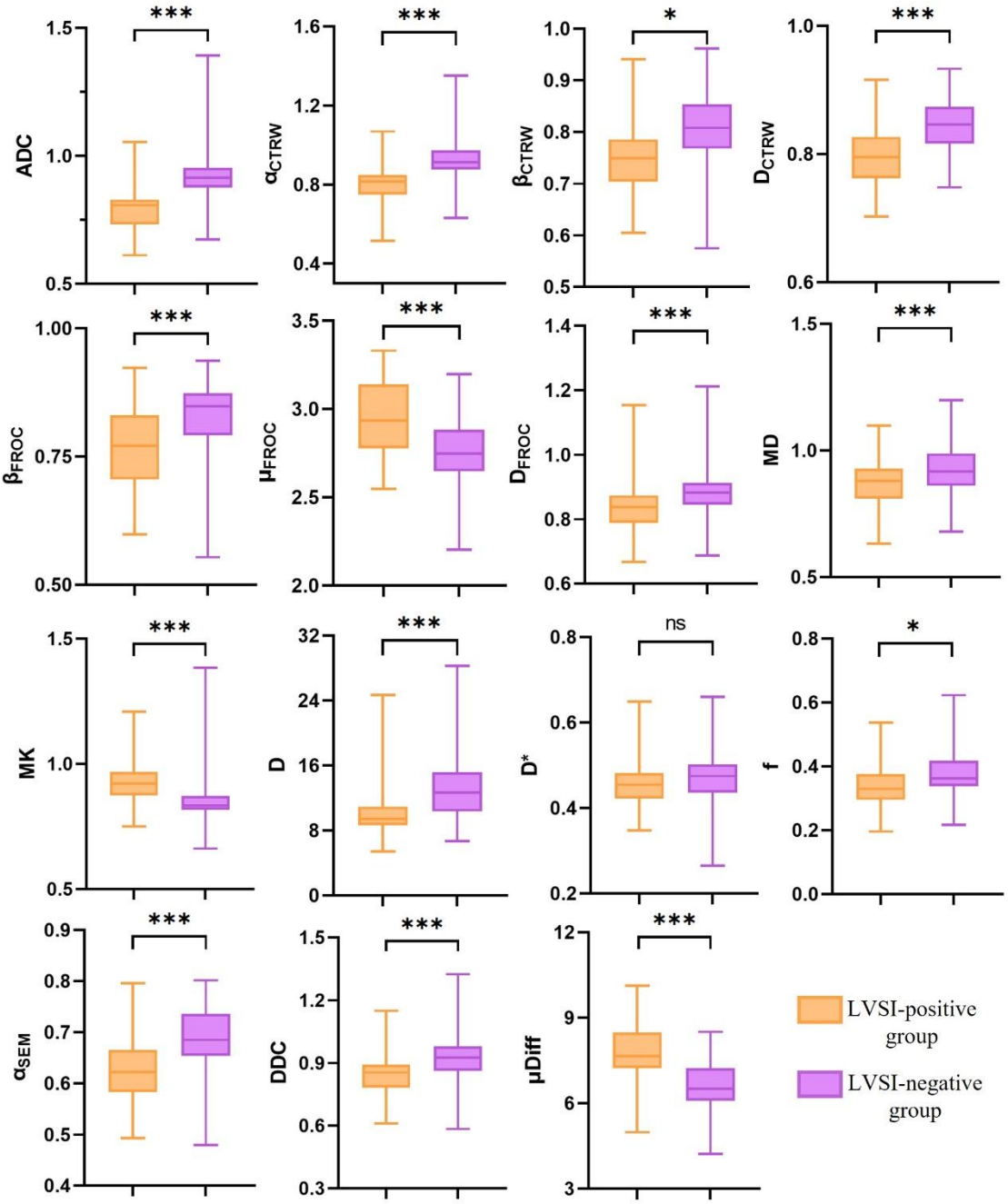



**Figure 2 Boxplots of diffusion parameters in LVSI-positive group and LVSI-negative group. ******P*< 0.001, **P*< 0.05, ns, not significant *P* ≥ 0.05. ADC, apparent diffusion coefficient; $\alpha_{CTRW}$, temporal diffusion heterogeneity index; $\beta_{CTRW}$, spatial diffusion heterogeneity index; $D_{CTRW}$, anomalous diffusion coefficient; $\beta_{FROC}$, fractional order derivative in space; $\mu_{FROC}$, spatial constant; $D_{FROC}$, diffusion coefficient; MD, mean diffusivity; MK, mean kurtosis; D, true diffusion coefficient; D*, pseudodiffusion coefficient; f, perfusion fraction; $\alpha_{SEM}$, intravoxel diffusion heterogeneity index; DDC, distributed diffusion coefficient; vMRE,

**virtual MR elastography.**

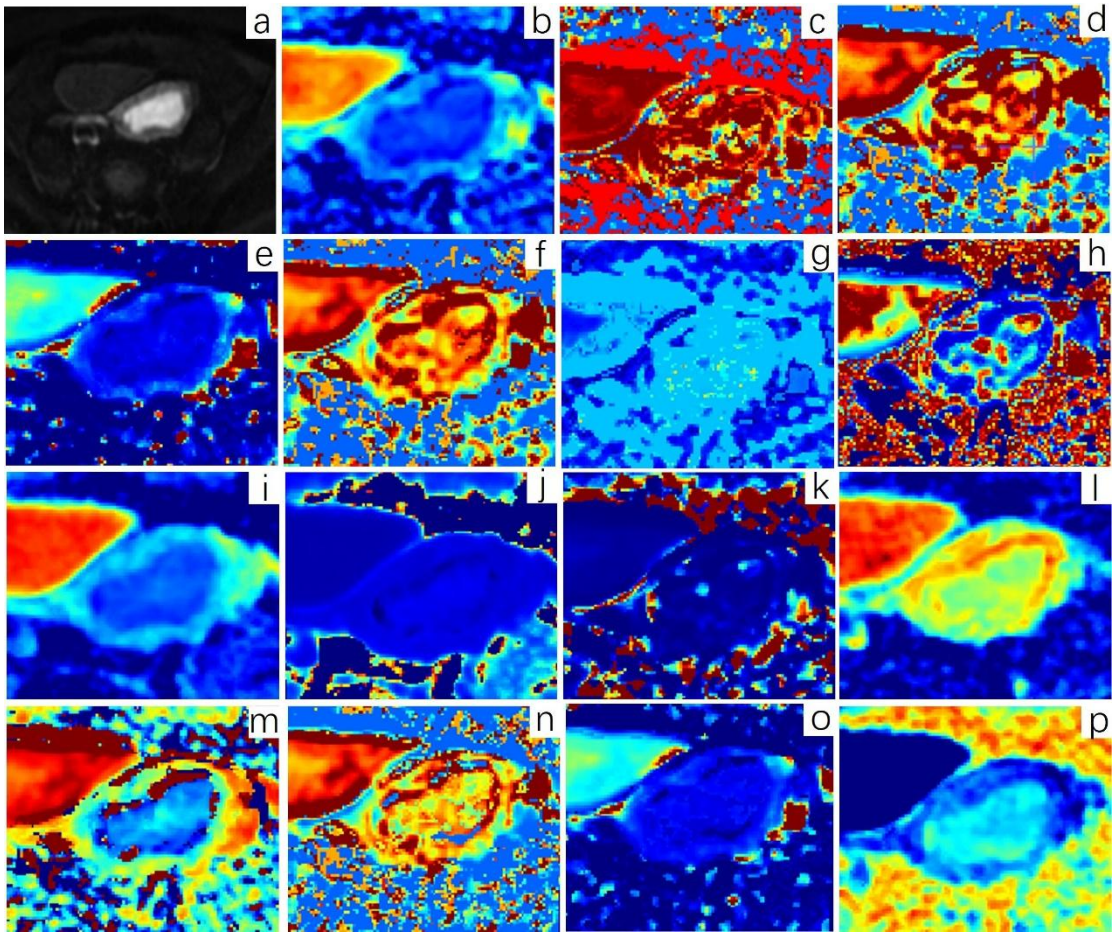



**Figure 3 DWI and multi-b-value DWI-derived images of a 67-year-old female with LVSI-positive uterine serous carcinoma. Marked hyperintensity is noted on the DWI image (a). Pseudocolor images demonstrate various multi-b-value DWI-derived maps:(b) ADC, apparent diffusion coefficient; (c) $\alpha_{CTRW}$, temporal diffusion heterogeneity index; (d) $\beta_{CTRW}$, spatial diffusion heterogeneity index; (e) $D_{CTRW}$, anomalous diffusion coefficient; (f) $\beta_{FROC}$, fractional order derivative in space; (g) $\mu_{FROC}$, spatial constant; (h) $D_{FROC}$, diffusion coefficient; (i) MD, mean diffusivity; (j) MK, mean kurtosis; (k) D, true diffusion coefficient; (l) D*, pseudodiffusion coefficient; (m) f, perfusion fraction; (n) $\alpha_{SEM}$, intravoxel diffusion heterogeneity index; (o) DDC, distributed diffusion coefficient; (p) vMRE, virtual MR elastography.**

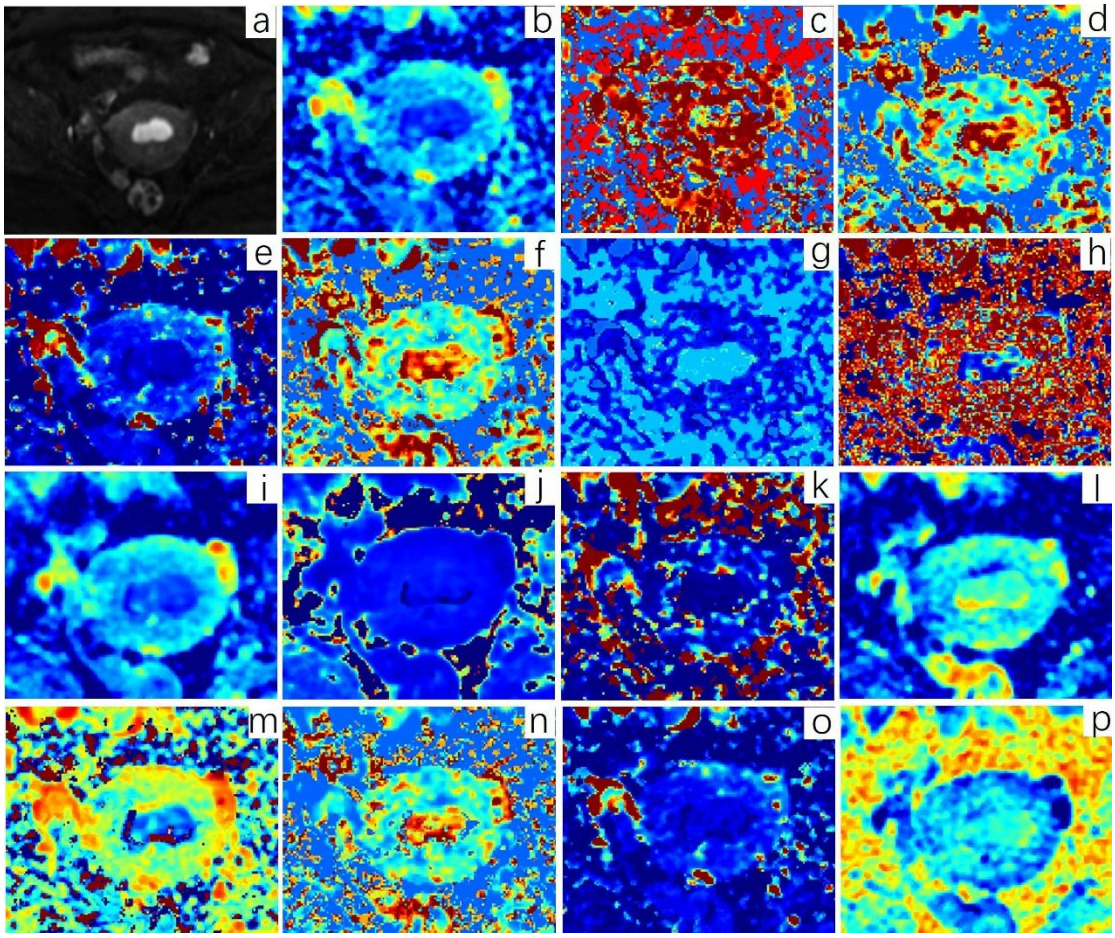



**Figure 4 DWI and multi-b-value DWI-derived images of a 61-year-old female with LVSI-negative endometrioid adenocarcinoma. (a) Marked hyperintensity is noted on the DWI image. Pseudocolor images demonstrate various multi-b-value DWI-derived maps:(b) ADC, apparent diffusion coefficient; (c) $\alpha_{CTRW}$, temporal diffusion heterogeneity index; (d) $\beta_{CTRW}$, spatial diffusion heterogeneity index; (e) $D_{CTRW}$, anomalous diffusion coefficient; (f) $\beta_{FROC}$, fractional order derivative in space; (g) $\mu_{FROC}$, spatial constant; (h) $D_{FROC}$, diffusion coefficient; (i) MD, mean diffusivity; (j) MK, mean kurtosis; (k) D, true diffusion coefficient; (l) D*, pseudodiffusion coefficient; (m) f, perfusion fraction; (n) $\alpha_{SEM}$, intravoxel diffusion heterogeneity index; (o) DDC, distributed diffusion coefficient; (p) vMRE, virtual MR elastography.**

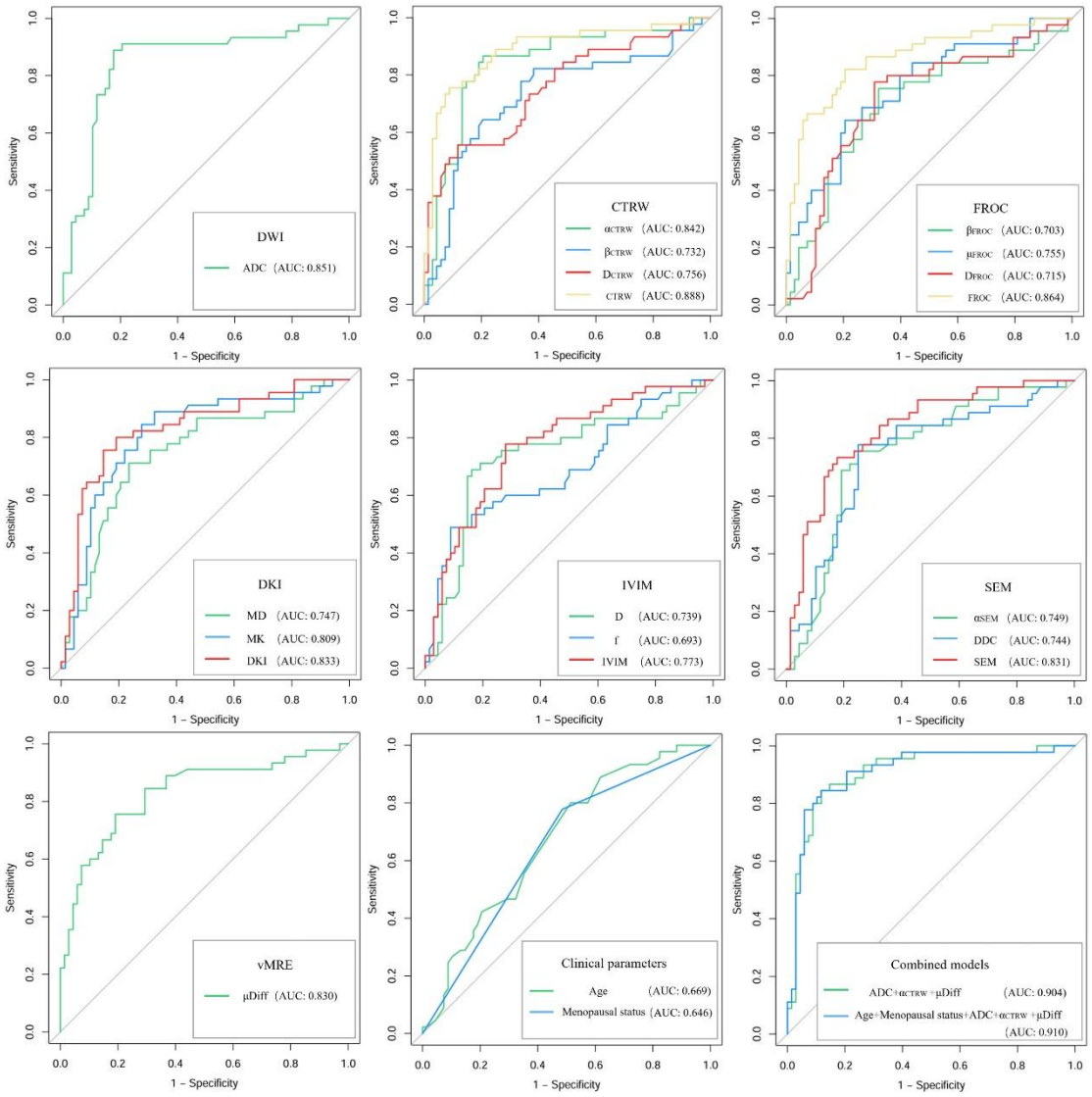



**Figure 5 Receiver operating characteristic curves for differentiating LVSI-positive group and LVSI-negative group. DWI, diffusion-weighted imaging; ADC, apparent diffusion coefficient; CTRW, continuous-time random walk; $\alpha_{CTRW}$, temporal diffusion heterogeneity index; $\beta_{CTRW}$, spatial diffusion heterogeneity index; $D_{CTRW}$, anomalous diffusion coefficient; FROC, fractional order calculus; $\beta_{FROC}$, fractional order derivative in space; $\mu_{FROC}$, spatial constant; $D_{FROC}$, diffusion coefficient. DKI, diffusion kurtosis imaging; MD, mean diffusivity; MK, mean kurtosis; D, true diffusion coefficient; D*, pseudodiffusion coefficient; f, perfusion fraction; SEM, stretched exponential model; $\alpha_{SEM}$, intravoxel diffusion heterogeneity index; DDC, distributed diffusion coefficient; vMRE, virtual MR elastography**.

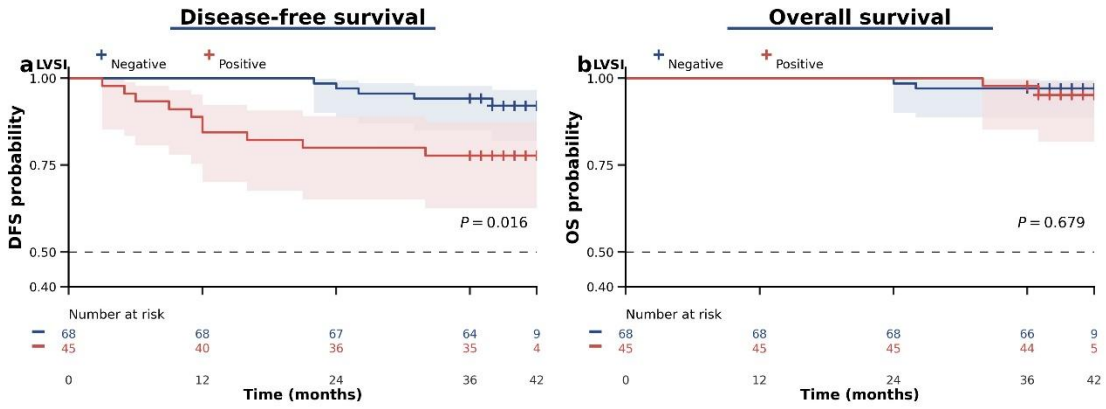



**Figure 6 Kaplan-Meier curve for disease-free survival and overall survival LVSI-positive group and LVSI-negative group.**

## Supplementary Files

This is a list of supplementary files associated with this preprint. Click to download.

- SupplementaryMaterial.docx